Ion velocity distributions in helicon wave plasmas: Magnetic field and pressure effects

T. Nakano,[a] K. P. Giapis,[b] R. A. Gottscho, T. C. Lee, and N. Sadeghi[c]
AT&T Bell Laboratories, Murray Hill, New Jersey 07974

(Received 3 June 1993; accepted 25 September 1993)

Consideration of ion transport in high density, low pressure plasma systems is important for meeting process requirements in the manufacturing of ultra-large-scale integrated circuits. The ion energy and angular distributions at the boundary between the plasma and the wafer, the sheath, influence etching selectivity, linewidth control, plasma-induced damage, and microscopic etching uniformity. These distributions, in turn, are easily altered by changing the magnetic field profile and/or the neutral gas pressure. Using Doppler-shifted laser-induced fluorescence, metastable ion velocity distribution functions in helicon-wave-excited Ar plasmas are measured. Two magnetic field configurations are examined. For a magnetic "mirror," where the field exhibits a maximum and a saddle point in the source, the plasma is observed to be asymmetric and nonuniform: this leads to broadened velocity distributions and significant ion drift from one region of the plasma to another. As the pressure is increased in the mirror field configuration, the transverse ion "temperature" exhibits a maximum as a function of pressure and, when etching is ion-flux limited, either decreasing or increasing the pressure should result in improved linewidth control. The plasma is more symmetric when the magnetic field is reversed in the source and again downstream. With this double cusp configuration, the transverse ion temperature decreases monotonically with pressure, and improved linewidth control in the ion-flux limit would be obtained by operating at higher pressure.

I. INTRODUCTION

New plasma sources operated at lower pressures and higher charge densities are being used in the manufacturing of ultra-large-scale integrated circuits.[1–5] Because of low pressure operation, these sources offer improved process uniformity and linewidth control while the use of high power excitation enables sufficient throughput for high volume manufacturing. Another advantage of using the new sources is improved ion energy control obtained by decoupling plasma generation from substrate biasing. Ion energy control is needed to optimize etching selectivity and anisotropy without compromising device yield or long-term reliability.

There are two critical aspects to effective ion energy control. First, the ion velocity spread parallel to the sheath electric field (perpendicular to the surface) should be relatively narrow compared to the mean parallel velocity. When this condition is met, the application of a bias voltage across the sheath can be used effectively to tune the mean ion energy. If the velocity spread were large, the high energy tail of the distribution could compromise etching selectivity and produce atomic displacement damage regardless of the bias voltage. Second, the ion velocity perpendicular to the sheath field (parallel to the surface) must be minimized; otherwise, linewidth control will be compromised.[6] Since the pressure is low and the charge density is relatively high in these sources, the sheath is collisionless. Thus, the ion velocity distribution function (ivdf) at the sheath edge and the sheath voltage completely determine the ivdf at the wafer surface.[7] The ivdf at the sheath edge, in turn, is controlled by the plasma properties, magnetic field profile, and the neutral gas density.

In this work, we extend previous studies of ivdfs in electron cyclotron resonance (ECR) and helicon wave excited plasmas.[8,9] We measure Ar^+ metastable ivdfs in helicon-wave-excited plasmas using Doppler-shifted laser-induced fluorescence (DSLIF). Electron density is also measured using microwave interferometry. The DSLIF experiment provides a direct measure of the ivdf along the laser propagation direction but averaged over the velocity components perpendicular to this direction. To obtain a truly one-dimensional ivdf along an arbitrary axis, one must resort to tomographic techniques that require optical access to the plasma beyond that possible in these experiments.[10] Nonetheless, the perpendicularly averaged ivdfs measured here provide a wealth of information on the plasma structure and dynamics. For example, the net drift velocity measured by DSLIF can be used to sample the electric field driving ions from one region of the plasma to another. In addition, if ionization is distributed over regions of nonuniform plasma, a distribution of velocity shifts will be observed and this will appear as a spread in the distribution function beyond the inherent spread caused by random ion motion. In general, a velocity shift signifies ion transport and nonuniform plasma. Velocity spread can signify hot ions and/or nonuniform plasma. By examining spreads and shifts as a function of position in the plasma, the steady-state structure of the plasma can be deduced and used to test the quantitative predictions of

[a]Permanent address: Department of Electrical Engineering, National Defense Academy, Yokosuka, Japan.
[b]Current address: Chemical Engineering Department, California Institute of Technology, Pasadena, CA.
[c]Permanent address: Laboratoire de Spectrometrie Physique, University Joseph Fourier and CNRS, Grenoble, France.

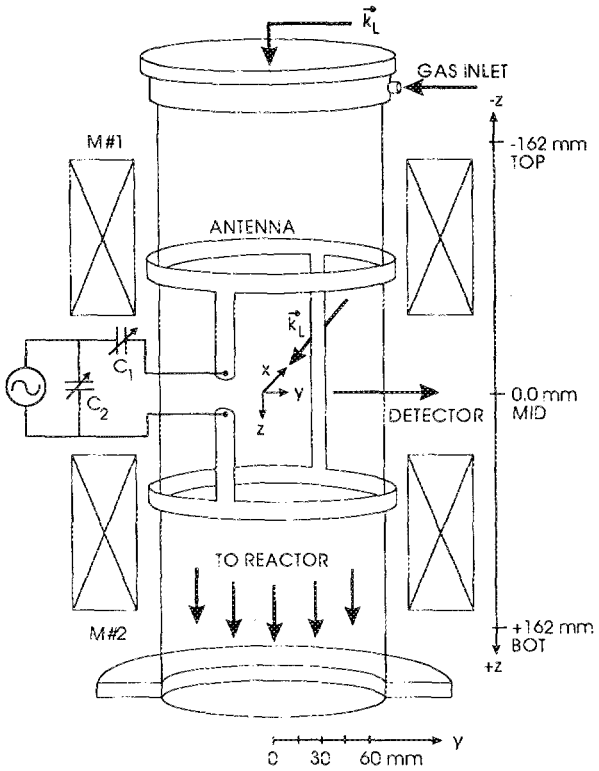

FIG. 1. Schematic representation of a helicon plasma source with gas inlet shown at the top. For some experiments, the gas inlet is placed downstream in the reactor (not shown, see Ref. 8).

plasma simulations.[11,12] The ivdfs determined here can also be used to guide etched profile simulation.[6,13]

Why examine metastable states in Ar plasmas? While Ar is usually only a constituent in processing plasmas, it is commonly used in diagnostic studies and computer simulations. In addition, we previously found only small quantitative differences between metastable ion transport in Ar and Cl_2; qualitatively, we found the systems to be similar.[8,9] Because the metastable state of Ar^+ should have a smaller charge exchange cross section with ground state neutral Ar,[8,9] the metastable ivdf can be a better indicator of plasma structure, and therefore a better test for plasma simulations than corresponding measurements of the ground state ivdf. Because metastable ions are more likely to be destroyed by quenching collisions than to alter their velocity by charge exchange, their ivdfs are more sensitive to changes in plasma potential; by contrast, the ground state ivdfs are often better described using the mobility limit in which case they provide more information about the local electric field to neutral density ratio.[14] While the metastable ivdf is not representative of the ground state ivdf, it is important to note that at lower pressures, the metastable flux to wafer surfaces can be a significant fraction ($\gtrsim 25\%$) of the total ion flux.[15]

Much of our previous work and similar work by Woods *et al.* focused on ion transport in ECR plasmas.[8,14] But, there are many other means by which high density (10^{11} cm^{-3}) plasma can be generated at low pressures (0.1–10 mTorr) and modest powers (1–3 kW).[1–3,5,16] Here, we consider plasma production using helicon waves.

TABLE I. Magnet dimensions.

Magnet	Height (cm)	Inner radius (cm)	Outer radius (cm)	No. turns	No. layers	No. windings
1	9.4	9.4	11.0	804	12	67
2	9.4	9.4	11.0	804	12	67
3	6.8	10.2	11.5	80	4	20
4	16	11.4	13.2	230	5	46

Helicon waves have been studied since the 1960s.[17–21] High density plasma production using helicon-wave excitation was reported in 1970 by Boswell,[21,22] who proposed that Landau damping played an important role in converting wave energy into electron kinetic energy.[21] Later, Chen calculated the mode structure of helicon waves and also emphasized the importance of Landau damping.[23,24] Evidence for Landau damping has been presented recently by Komori *et al.*[25] and Lowenhardt *et al.*[26] Most of these studies of wave propagation and coupling have been carried out in uniform magnetic fields.

In plasma processing, helicon sources have been used mostly for etching in nonuniform magnetic fields. Bouchoule *et al.* first reported etching of Si with a so-called resonantly inductive plasma excitation (RIPE) source.[27] Subsequently, Boswell and Porteous[28] further investigated the SF_6 plasma etching of Si and Perry and Boswell showed that Si can be anisotropically etched at a rate of 0.7 μm/min with a selectivity to SiO_2 of 5.[29] More recently, helicon source plasmas have been used for etching Al,[30] SiO_2,[31] and W.[32] Recent results have shown that cusp configurations are beneficial in enhancing both plasma density[33] and process uniformity.[34]

Besides our preliminary work,[9] Charles *et al.*[35] have examined ion energy distribution functions (iedf) on axis but downstream from a magnetic field-free plasma excited with a helicon antenna. The total ion iedf was sampled using a grounded probe and gridded energy analyzer as a function of pressure and distance from the source and analyzed taking into account the drift in an ambipolar electric field and the effects of charge exchange collisions. In this work, we report measurements of both the parallel and perpendicular metastable ivdfs as a function of axial and radial position in the source for a range of pressures and two different magnetic field configurations.

II. EXPERIMENTAL DETAILS

A. Helicon source

A schematic representation of the helicon plasma system used in this work is shown in Fig. 1; further details can be found elsewhere.[9,15] The system consists of a quartz-tube source and a stainless-steel reactor into which the plasma expands. In the source, the magnetic field profile is controlled using two electromagnets with currents I_1 and I_2; a third magnet is placed at the throat of the reactor to control transport with current I_3 into the reactor. The

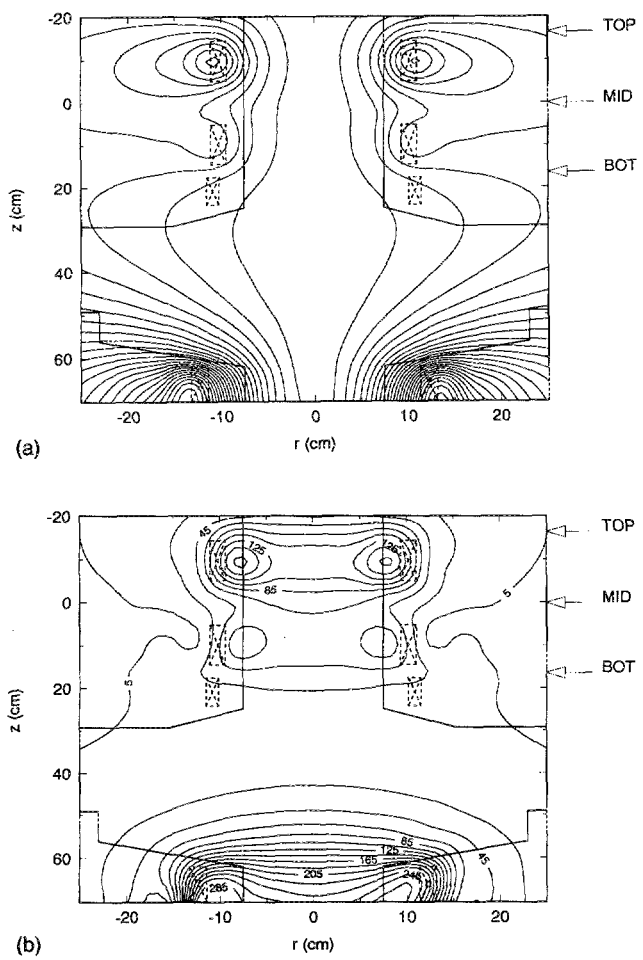

FIG. 2. Magnetic field flux lines (a) and field magnitude (b) for the mirror configuration: $I_1/I_2/I_3/I_4=2.5/1/0/25$ *A*. The outlines of the magnet coils, the chamber walls, and the measurement positions TOP, MID, and BOT along $\hat{z}$ are all shown. Note that the vertical scale ($\hat{z}$) is compressed with respect to the horizontal scale ($\hat{x}$).

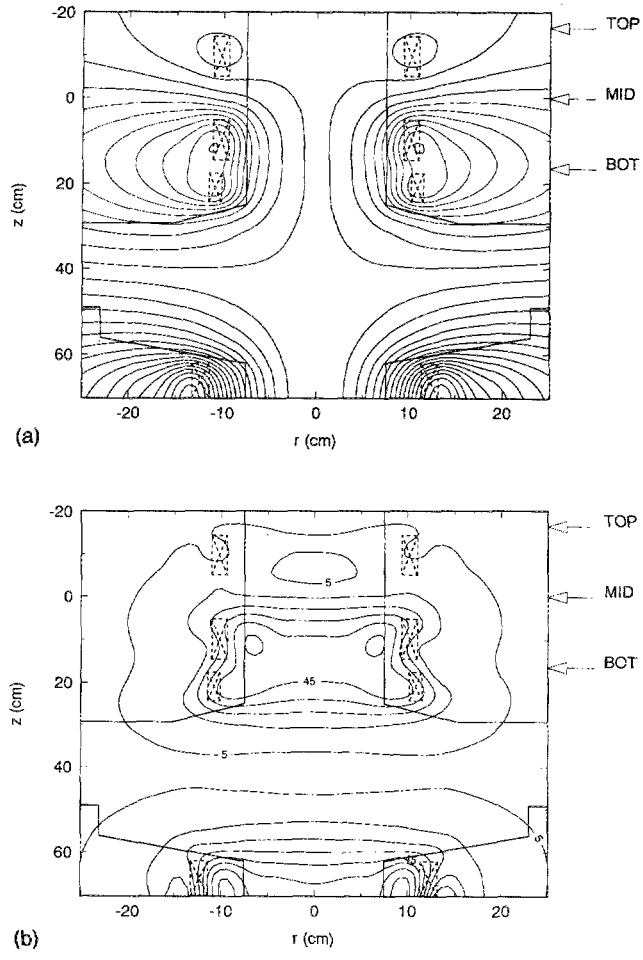

FIG. 3. Same as Fig. 2 except for the double-cusp configuration: $I_1/I_2/I_3/I_4=-0.2/0.8/-6/7$ *A*. The outlines of the magnet coils, the chamber walls, and the measurement positions TOP, MID, and BOT along $\hat{z}$ are all shown. Note that the vertical scale ($\hat{z}$) is compressed with respect to the horizontal scale ($\hat{x}$).

magnetic field profile in the reactor is controlled using I_3 and the current I_4 in a fourth electromagnet placed below a wafer platen. The magnet characteristics, dimensions, windings, and layers, are given in Table I; typical field contours and flux lines are shown in Figs. 2 and 3.

In our previous work, the system was operated as a weak magnetic mirror, where the field strength exhibits a maximum near the top of the reactor and a saddle point before the source joins the reactor (Fig. 2). In this work, we compare the results obtained with the weak mirror to those obtained with the double-cusp magnetic field profile, where the field is reversed near the top of the source and again in the reactor (Fig. 3). Note that for the double cusp, the field is nearly uniform from the lower-half of the source to the throat; but, for the mirror, the field is diverging and nonuniform in this region.

The plasma is excited by applying a rf field to one of two types of antenna. In our previous work, we used copper strips glued to the source tube in a "Boswell" configuration [Fig. 3(a) in Ref. 9]. In this work, we used a rigid, Nagoya type III antenna originally provided by Lucas Labs and modified by us. We found no significant differences in the Ar^+ metastable ivdfs between the two antennas. The primary difference observed was in the electron density versus power dependence; with the Boswell antenna, we found discontinuities and hysteresis as the electron density was measured as a function of rf power. For the Nagoya type III, sudden changes in electron density were observed at similar power levels, but hysteresis and discontinuity were less apparent. It should be noted that since we have made no attempt to measure the wave field, we cannot be certain that a helicon wave has been excited. However, in similar systems using similar antennas, the wave field has been measured and attributed to a helicon mode.[25,36]

Radio frequency (rf) power (PlasmaTherm HFS 2500D) is supplied to the antenna through a matching network consisting of two variable vacuum capacitors. Gas flow is actively controlled using a Tylan General 80-4 mass flow controller; pressure is controlled by changing gas flow rate, no throttling valve on the turbomolecular pump is used. The gas is injected either into the source or into the reactor. Unless otherwise stated, the gas is injected into the source. Pressure is monitored in the reactor out of sight of the plasma using a 1 mTorr (0.133 Pa) Baratron head

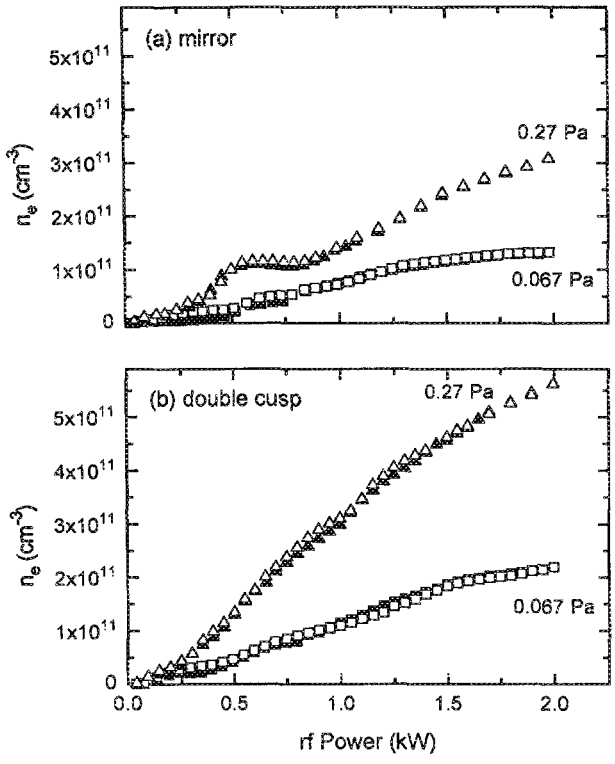

FIG. 4. rf power dependence of electron density n_e at the MID position (z=0 cm) for (a) mirror and (b) double-cusp configurations. The pressures are indicated. Open figures correspond to systematically increasing power while closed figures correspond to decreasing power. Note that there is some hysteresis observed for both configurations but the effects are small.

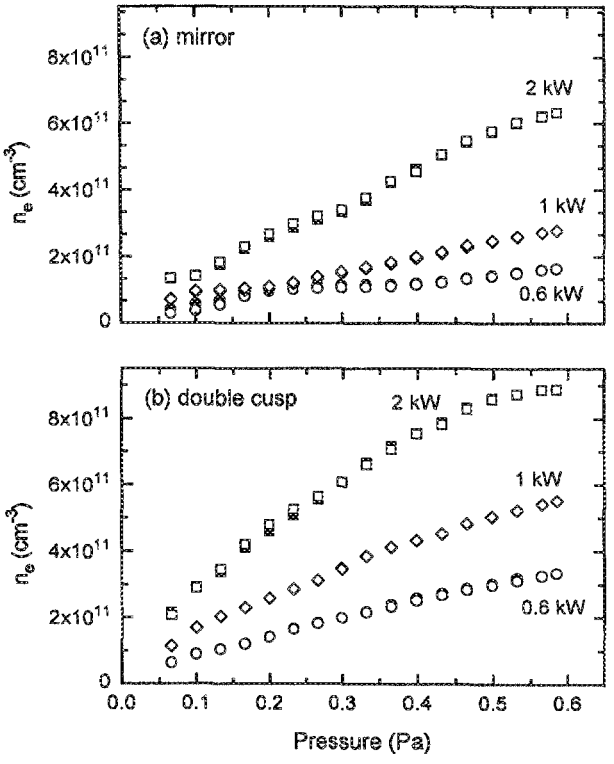

FIG. 5. Pressure dependence of n_e, at the MID position (z=0 cm) for (a) mirror and (b) double-cusp configurations. The rf powers are indicated.

(MKS 227A). The system base pressure is $\sim 4\times10^{-5}$ Pa (3×10^{-7} Torr).

B. DSLIF measurements

For the DSLIF measurements, we use a Coherent 699-29 ring dye laser with an integral wavemeter. Pumping with a continuous wave (cw) Ar^+ laser, a single longitudinal mode of the dye laser is obtained with linewidth of 1 MHz. Computer-controlled scanning over Doppler profiles is precise to 10^{-4} nm. After passing through 130 m of AT&T 62.5 μm diam core, multimode optical fiber from one laboratory to another, the unpolarized laser light is collimated, modulated, and brought to the reactor along either the x or z directions (Fig. 1). The $4p'\ ^2F_{7/2}\leftarrow 3p^4 3d\ ^2G_{9/2}$ transition at 611.49 nm is excited and the ion velocity along the laser propagation direction is directly proportional to the Doppler shifted absorption frequency ν according to:

$$\nu=\nu_0(1-v_j/c), \tag{1a}$$

$$I(\nu)d\nu=Knf(v_j)dv_j, \tag{1b}$$

where ν_0 is the line-center (rest velocity) absorption frequency; v_j is the ion velocity along the laser propagation direction; j denotes either $\hat{x}$ or $\hat{z}$; c is the speed of light; and n is the metastable ion density. $I(\nu)d\nu$ is the LIF excitation line profile, and K is an apparatus constant. The one-dimensional ivdf, $f(v_j)$, is an average over the two perpendicular velocity distribution functions. For example,

$$f(v_x)=\int\int f(v_x,v_y,v_z)dv_y\,dv_z. \tag{1c}$$

Velocity resolution is limited by a combination of natural and power broadening; from saturation spectroscopic experiments, we estimate the homogeneous linewidth to be $\lesssim 0.003$ cm^{-1} which corresponds to $\Delta v_j \approx 0.06$ km/s.

Laser-induced fluorescence is detected from the $4p'\ ^2F_{7/2}\rightarrow 4s'\ ^2D_{5/2}$ transition at 460.96 nm at right angles to the laser propagation direction and focused onto a slit-shaped, fiber-optic bundle (General Fiber Optics) using a 75 mm focal length, 50 mm diam lens. The other end of the bundle is also slit shaped and imaged onto the entrance slit of a 1.25 m scanning monochromator (Spex 1269) equipped with a Hamamatsu R376 photomultiplier tube, whose output is fed into a phase-locked amplifier. Spatial resolution is dictated by bundle dimensions, lens focal length, and lens placements: for v_z ivdf measurements, $\Delta z \approx 1$ mm and $\Delta x \approx 5$ mm, while for v_x ivdfs, $\Delta z \approx 5$ mm and $\Delta x \approx 1$ mm. The finite laser beam diameter gives a resolution along the detector direction of $\Delta y \approx 2$ mm.

The detector lens and laser beam are positioned using translational stages along x, y, and z directions at the TOP, MID, and BOT positions (see Fig. 1). However, when the ivdf-sampled point is moved from the MID to the TOP or BOT, the stages are moved and the lens and laser beam are

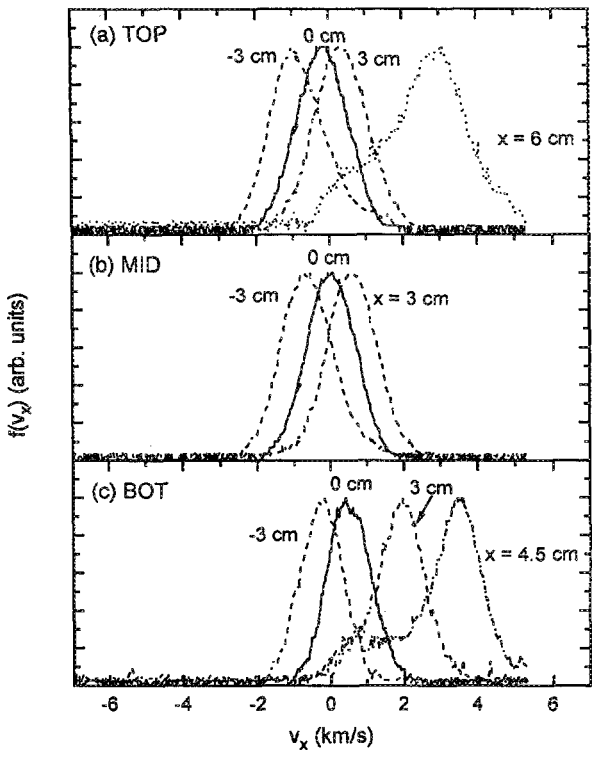

FIG. 6. Transverse, v_x ivdfs at 0.067 Pa as a function of x and z for the mirror configuration. rf power is 1 kW.

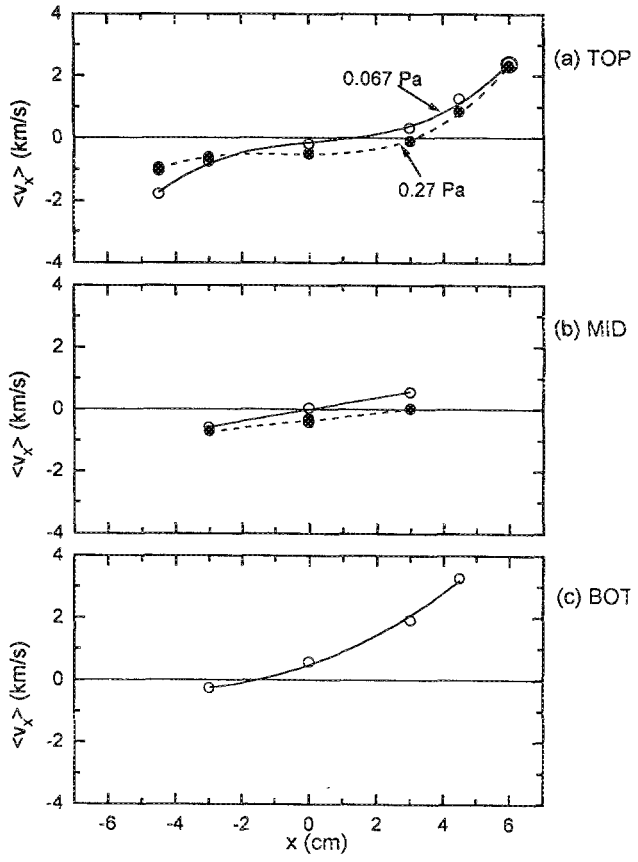

FIG. 7. Average transverse velocity $\langle v_x \rangle$ as a function of x and z for two different pressures in the mirror configuration. Note that because of the strongly divergent field at the BOT position and consequent wall loss, the DSLIF signal could not be observed at the higher pressure. Also, because of the plasma asymmetry, signals are weaker toward negative x.

realigned. The accuracy of the alignments is ~ 1 mm at the MID and ~ 5 mm at the TOP and BOT in the z direction, and ~ 1 mm along the x and y directions regardless of the z position.

DSLIF spectra are stored digitally and then converted to one-dimensional ivdfs by transforming the frequency scale to a velocity scale according to Eq. (1a). Moments of the ivdfs are then computed to obtain relative density, average velocities, random energy, and ivdf asymmetry.

C. Electron density measurement

Electron density n_e is measured using a 35 GHz microwave interferometer (PMT DDM-01-B) at the MID position. The measurement is sensitive to placement and alignment of the horn antennae so that the absolute values of n_e are believed to be accurate to no better than a factor of 2. Consistent with our previous work,[15] the values for n_e shown here are upper limits and may be as much as two times too large.

III. RESULTS AND DISCUSSION

A. Electron density versus power and pressure

The electron density at the MID position monotonically increases with rf power and Ar pressure for both mirror and double-cusp configurations. The data shown in Figs. 4 and 5 are obtained using the Nagoya type III rigid antenna. As observed with the Boswell antenna, small hysteresis appears over a limited range as the power or pressure are first increased and then decreased, but in contrast with our results obtained with the Boswell antenna, no discontinuous density jumps are discernible.

For the same pressure and power, n_e at the MID position is always larger for the double-cusp magnetic field profile. The charge density is determined by the balance between distributed, gas-phase ionization and wall loss: Volume losses can be neglected at these charge densities and pressures. The wall loss, in turn, is reduced by reducing the flux of electrons to the wall by using a confining magnetic field. By forming cusps, the plasma electrons will be reflected from the regions of stronger field near the walls at the top of the source. The reduced loss and consequent increase in n_e is amplified by the plasma as the ionization rate will increase with the increase in n_e.

In the comparisons between the mirror and double cusp configurations below, we note that the rf power is set to 1 and 1.5 kW, respectively. While we would have preferred keeping the rf power constant, we find that the mirror plasma is not stable at 1.5 kW and the double-cusp plasma is not stable at 1.0 kW. In addition, we feel that these power levels ensure that we are working in the so-called "high" mode for both configurations.[29]

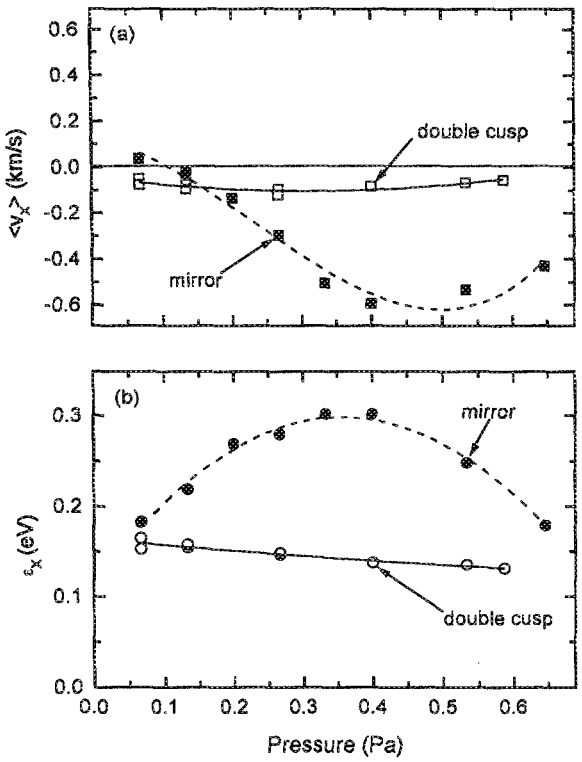

FIG. 8. Variation in (a) $\langle v_x \rangle$ and (b) ε_x as function of pressure for both the mirror and double-cusp configurations. The data are obtained at $x=y=z=0$.

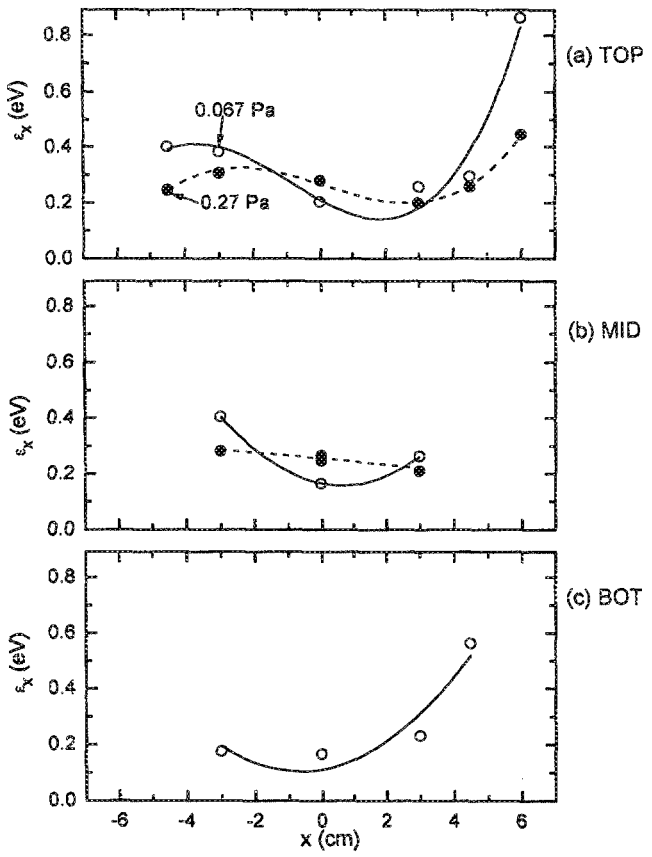

FIG. 9. Random transverse ion energy ε_x as a function of x and z for two different pressures in the mirror configuration. Note that because of the strongly divergent field at the BOT position and consequent wall loss, the DSLIF signal could not be observed at the higher pressure. Also, because of the plasma asymmetry, signals are weaker toward negative x.

B. Transverse ivdfs

1. Mirror configuration

Monitoring the transverse ivdf in the source and understanding how it varies with conditions and position is important for predicting and controlling linewidths during submicron etching. Transverse energy gained in the source can be easily transported to device wafers.

Typical v_x ivdfs at 0.067 Pa for the mirror configuration are shown in Fig. 6. It is clear that the ivdfs are not symmetric with respect to reflection through the yz plane, i.e., about $x=0$. For example, the ivdf at $x=0$ cm is not centered about $v_x=0$ at the TOP and BOT positions and there is a clear lack of symmetry between the ivdfs at $x=+3$ and -3 cm.

This lack of symmetry is seen clearly when the average velocity $\langle v_x \rangle$ is plotted as a function of position (Fig. 7) or pressure [Fig. 8(a)]. When the average velocity is zero, there is probably an intense source of ionization such that the electric field is zero, corresponding to a maximum in the plasma potential. Assuming that ions are born from neutrals with no net motion, then little or no net velocity will be discernible when the ionization rate is much larger than the rate at which ions are transported into and out of the field of view by drift and diffusion. Alternatively, if the plasma potential is a local maximum, the local field will be zero, the ion density will also be a maximum, and the net ion velocity will be zero. If the plasma were axisymmetric, we would not expect to see a net velocity shift on-axis, since even off-axis density maxima would symmetrically feed the on-axis density distribution from all directions equally and thus produce a symmetrical, unshifted ivdf. Observation of a net shift on-axis necessarily implies that the discharge is not axisymmetric and either the wall losses or the bulk ionization rate are not axisymmetric. As shown in Fig. 7, the asymmetry is more apparent at higher pressure: For example, the x position where $\langle v_x \rangle$ is zero shifts systematically to larger values of x as the pressure is increased and reaches 3 cm at 0.27 Pa. At 0.65 Pa (not shown in Fig. 7), $\langle v_x \rangle = 0$ at $x=5$ cm, only 2.6 cm from the wall. Plasma asymmetry is further evident when one examines $\langle v_x \rangle$ as a function of pressure at $x=y=z=0$ [Fig. 8(b)]. The average speed along $\hat{x}$ increases, toward negative values of x, as the pressure is increased.

Asymmetry in the mirror plasma appears as two columns along z at approximately $x=\pm 5$ cm and $y=0$ cm, i.e., along lines in the xz plane, that are visibly more intense. The $+5$ cm column is visually brighter than the -5 cm column, consistent with the observed net shift in the v_x ivdf.

It should be recognized that the helicon source need not be axisymmetric. The antennae used are not axisymmetric and application of a magnetic field destroys axisymmetry. Nonetheless, to better understand the origin of the asym-

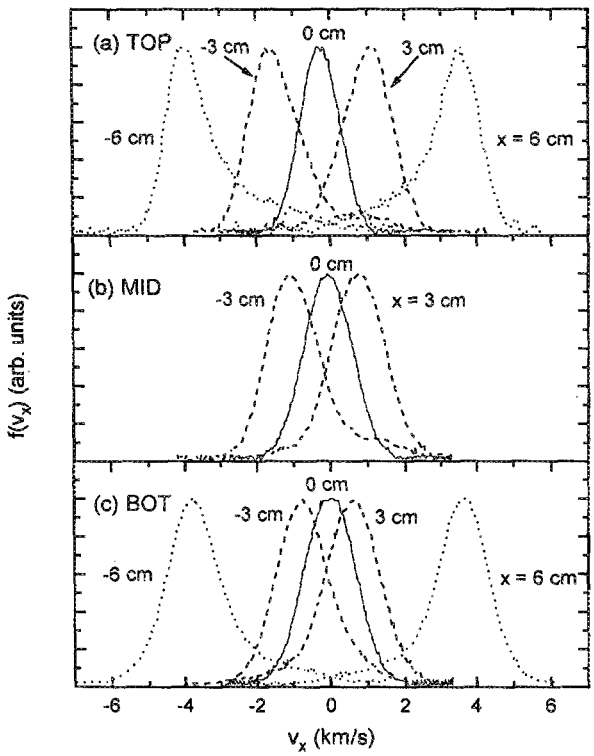

FIG. 10. Transverse, v_x ivdfs at 0.067 Pa as a function of x and z for the double-cusp configuration. rf power is 1.5 kW.

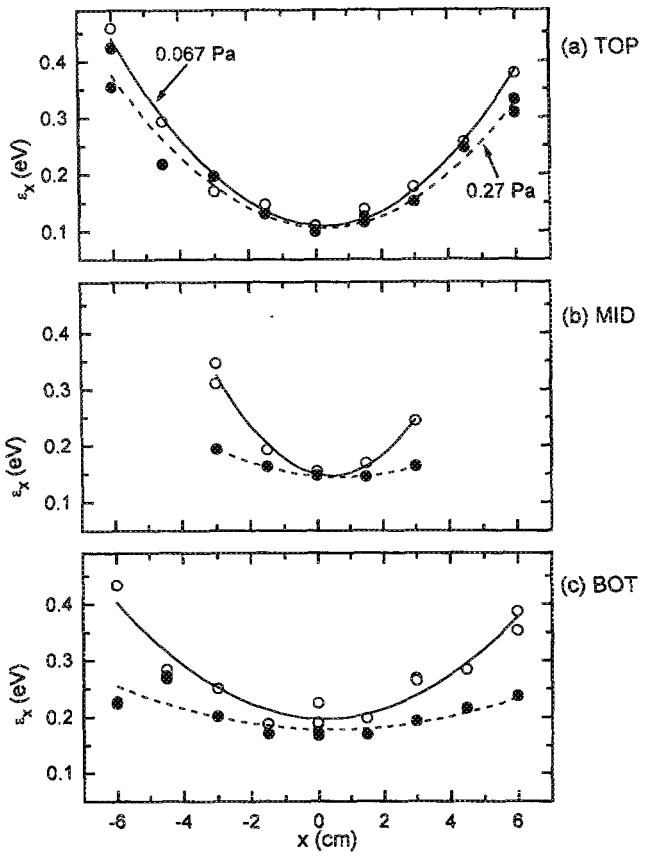

FIG. 12. Random transverse ion energy ε_x as a function of x and z for two different pressures in the double-cusp configuration.

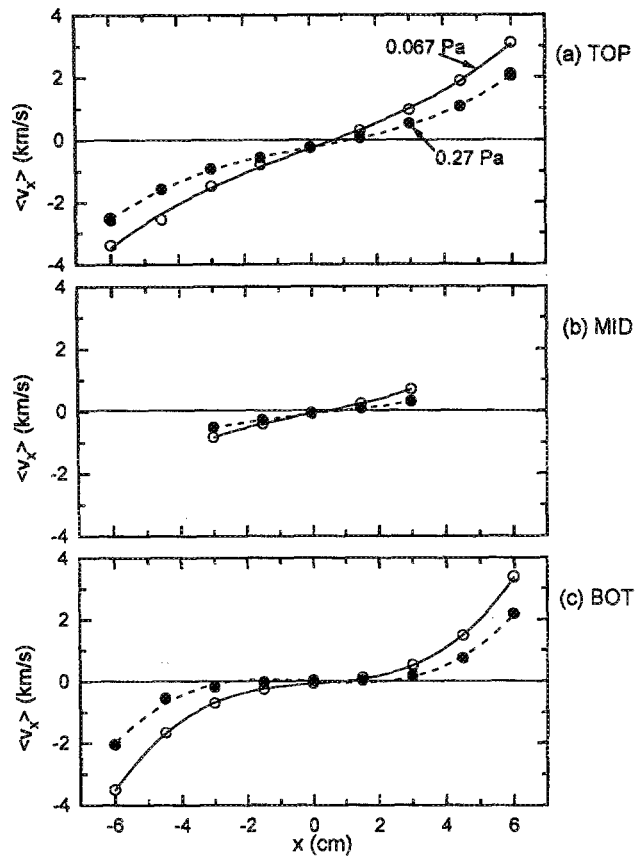

FIG. 11. Average transverse velocity $\langle v_x \rangle$ as a function of x and z for two different pressures in the double-cusp configuration.

metry, we varied the position of the gas inlet and the orientation of the antenna. Although the integrated DSLIF intensities do vary, the ivdfs do not change significantly with the gas inlet position. Similarly, rotation of the antenna did not noticably alter the positions of the bright columns or the magnitudes of $\langle v_x \rangle$.

The random transverse ion energy is given by

$$\varepsilon_x = M\langle (v_x - \langle v_x \rangle)^2 \rangle, \tag{2}$$

where M is the ion mass. Note that if the ivdf is Gaussian, $\varepsilon_x = kT_x$. Random ion energy can result from collisions with neutrals that convert directed energy into random energy or by formation of ions in a spatially varying potential. In both cases, the ivdf will be broadened relative to the collisionless limit where ions are formed in a uniform potential. As shown in Fig. 9, there is clearly an increase in ε_x near the source walls. This is also evident from the ivdfs plotted in Fig. 6, where the bimodality is consistent with a slow component produced by local ionization and a fast component produced by ions drifting toward the wall from a region of higher potential. Note that the random ion energy on-axis is 0.1–0.3 eV [Figs. 8(b) and 9]. For ion-flux limited etching reactions, such large transverse ion energies would dictate the application of a ~50 eV bias voltage to obtain ~50% of the ion energy flux within 5° of normal incidence.[7]

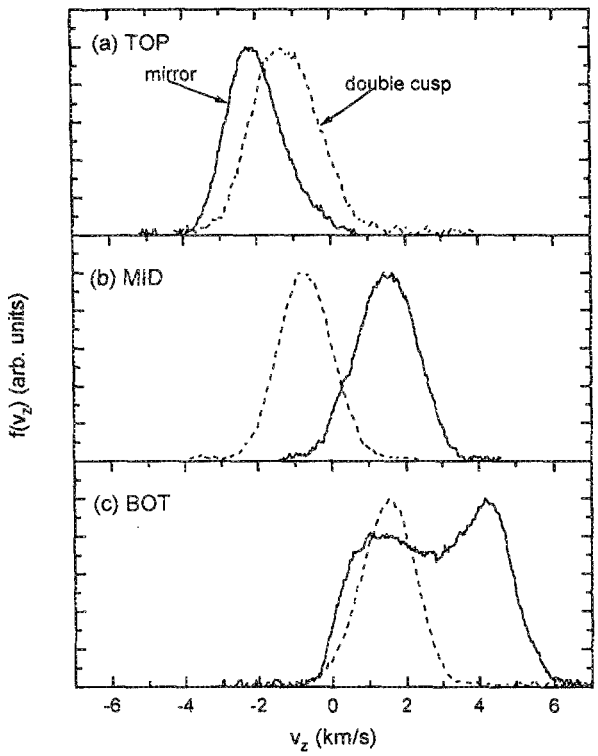

FIG. 13. Parallel, v_z ivdfs at 0.067 Pa as a function of z at $x=y=0$ for the mirror (solid) and double-cusp (dashed) configurations.

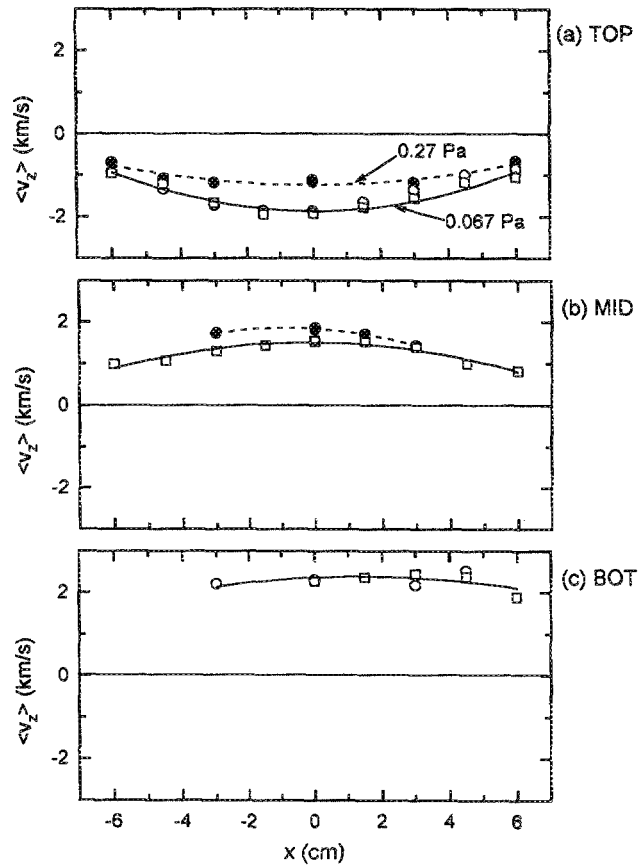

FIG. 14. Average parallel velocity $\langle v_z \rangle$ as a function of x and z for two different pressures in the mirror configuration. Note that because of the strongly divergent field at the BOT position and consequent wall loss, the DSLIF signal could not be observed at the higher pressure. Also, because of the plasma asymmetry, signals are weaker toward negative x. For the data at 0.067 Pa, the squares correspond to measurements made along $\hat{y}$ instead of $\hat{x}$. For the $f(v_z)$ measurements, little difference is observed between variations along $\hat{x}$ vs $\hat{y}$ axes.

Note that ε_x exhibits a maximum as a function of pressure [Fig. 8(b)]. While the data in Fig. 8(b) are for $x=y=z=0$ at 1 kW, this trend is observed throughout the source at several powers. The initial increase in ε_x is consistent with the increasing asymmetry and nonuniformity in the plasma, as evident in the changes in $\langle v_x \rangle$ [Figs. 7 and 8(a)]. In addition, the increase in pressure will increase elastic scattering that can convert directed motion along $\hat{x}$ or $\hat{z}$ into random motion. At higher pressures, quenching collisions may destroy ions before they can drift from one plasma potential to another and thereby reduce ε_x. Additionally, elastic and charge exchange collisions will tend to equilibrate the ivdf with the neutral velocity distribution function. In any case, the maximum in ε_x suggests that linewidth control would be most difficult to achieve at intermediate pressures.

2. Double-cusp configuration

Switching to the double-cusp magnetic field configuration (Fig. 3), we find that the bright columns are no longer visually evident and the ivdfs are more symmetric about the yz plane (Fig. 10). However, $\langle v_x \rangle$ is still finite at $x=0$ [Figs. 8(a) and 11]. As for the mirror configuration (Fig. 6), the off-axis ivdfs for the double-cusp configuration (Fig. 10) are shifted and skewed toward smaller velocities with both skew and shift systematically increasing with increasing $|x|$. Again, the shapes of these distributions are consistent with two velocity components, a slow one created by local ionization and a fast one created by drift from a region of higher potential. Since $\langle v_x \rangle$ crosses zero only near the center of the source, the plasma density must be a maximum near the center of the source tube. If the density were a maximum off-axis, $\langle v_x \rangle$ would be zero off-axis and not near $x=0$, as in the mirror configuration. Similarly, if there were two symmetrically situated density maxima, one would expect $\langle v_x \rangle$ to exhibit three zero crossings: one for each maximum and one on-axis where the drift from each density maximum is cancelled by drift from the other maximum. The existence of only one density maximum is consistent with volume loss being negligible compared to wall loss.

At the TOP position, the double-cusp plasma uniformity appears to be comparable to the mirror plasma uniformity [compare Figs. 7(a) and 11(a)]. But, at the MID and BOT positions, where the magnetic field is more uniform (Figs. 2 and 3) the double-cusp plasma is clearly more uniform as well as more symmetric.

The improved uniformity in the double-cusp plasma is further evident in the values for ε_x [Figs. 8(b) and 12]. Note the change in scales from Fig. 9 to Fig. 12. Most striking is the monotonic decrease in ε_x with increasing pressure for the double cusp plasma as opposed to the

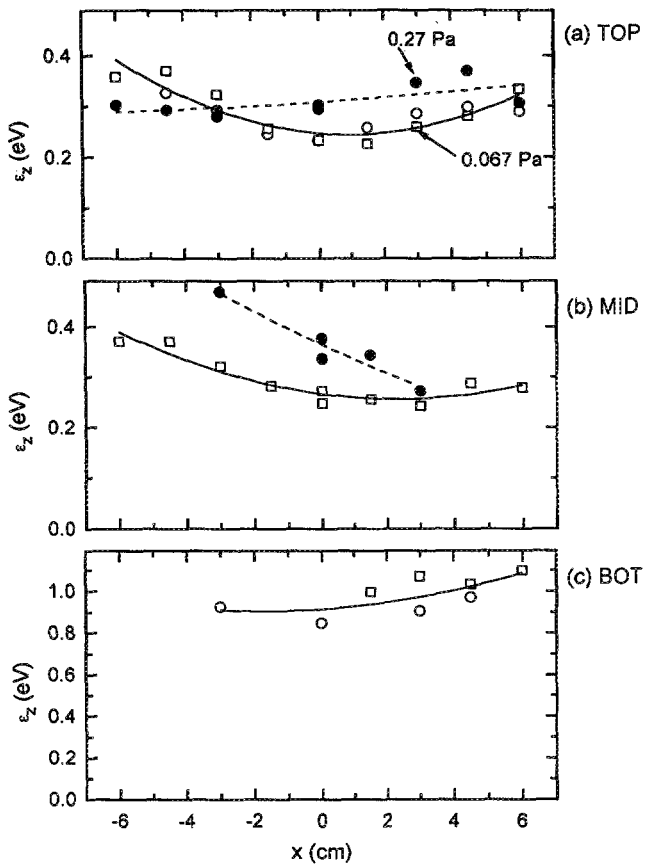

FIG. 15. Random parallel ion energy ε_z, as a function of x and z for two different pressures in the mirror configuration. Note that because of the strongly divergent field at the BOT position and consequent wall loss, the DSLIF signal could not be observed at the higher pressure. Also, because of the plasma asymmetry, signals are weaker toward negative x. For the data at 0.067 Pa, the squares correspond to measurements made along $\hat{y}$ instead of $\hat{x}$. For the $f(v_z)$ measurements, little difference is observed between variations along $\hat{x}$ vs $\hat{y}$ axes.

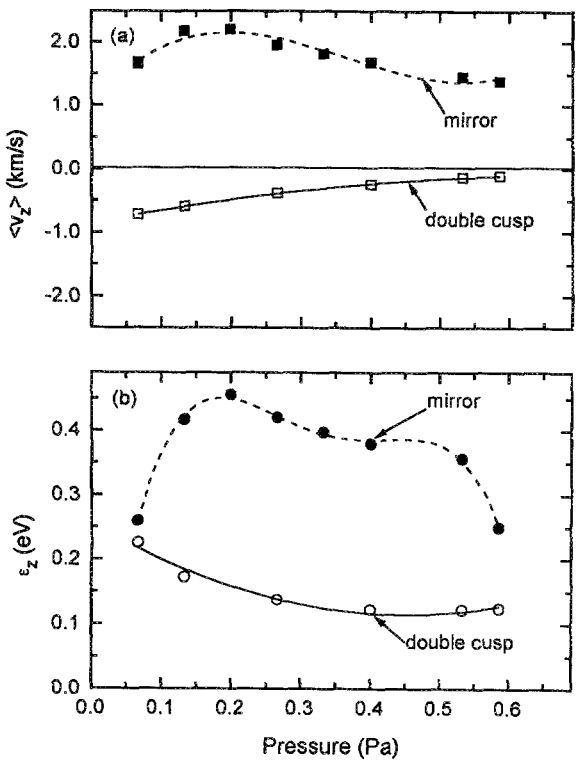

FIG. 16. Variation in (a) $\langle v_z \rangle$ and (b) ε_z as function of pressure for both the mirror and double-cusp configurations. The data are obtained at $x=y=z=0$.

maximum observed for the mirror plasma. From the spatial variation in $\langle v_x \rangle$ (Fig. 11) and ε_x (Fig. 12), it is clear that the double-cusp plasma uniformity improves with increasing pressure and the spread in transverse ion energy decreases accordingly. Thus, for etching limited by ion energy flux, both linewidth control and etching uniformity should be improved by increasing pressure.

C. Parallel ivds

1. Mirror configuration

Typical ivdfs along $\hat{z}$ are shown in Fig. 13. Two features are most evident: (1) the direction of ion transport is reversed between the TOP and MID positions and (2) the ivdf at the BOT position is very broad and clearly bimodal. These features have been discussed previously[9] and are observed for both Ar and Cl_2 plasmas. The change in direction for the ion drift implies that the plasma density and potential must go through a maximum between the TOP and MID positions. Note that the magnetic field also exhibits a maximum between these positions (Fig. 2). The bimodal distribution at the BOT position is consistent, again, with a slow component formed by local ionization and a fast component drifting from a region of higher potential.

The radial variations in $\langle v_z \rangle$ and $\varepsilon_z = M\langle (v_z - \langle v_z \rangle)^2 \rangle$ are shown in Figs. 14 and 15, respectively. The decrease in $\langle v_z \rangle$ toward the walls is consistent with enhanced ionization off-axis, as discussed above for the transverse ivdfs. The asymmetry in the plasma is more evident in the plots of ε_z. Note the large values for $\langle v_z \rangle$ and ε_z at the BOT position are consistent with the strongly diverging field at this position (Fig. 2). In fact, the ion loss to the walls is large and the signal to noise is so small that metastable ions could not be detected at the position for pressures above 0.067 Pa.

As a function of pressure, the changes in $\langle v_z \rangle$ and ε_z at $x=y=z=0$ are similar to those observed for $\langle v_x \rangle$ and ε_x, respectively (compare Figs. 8 and 16). The initial increase in $\langle v_z \rangle$ indicates that the potential gradient increases and that ions gain more energy between collisions despite the reduction in mean free path at the higher pressure. As the plasma becomes less uniform, ion formation occurs over a distributed potential and, as we have already discussed, this will broaden the ivdf as ions stream into the field of view from regions of different potential. In addition, elastic collisions may convert directed motion along $\hat{z}$ and $\hat{x}$ to random energy along both directions. At higher pressures, quenching and charge exchange help to cool the ivdfs and reduce the drift velocity.

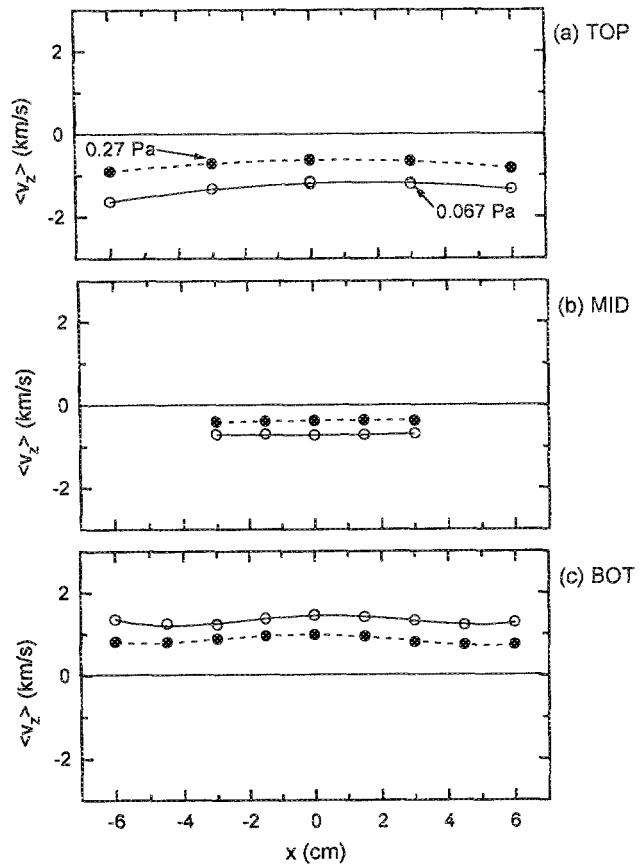

FIG. 17. Average parallel velocity $\langle v_z \rangle$ as a function of x and z for two different pressures in the double-cusp configuration.

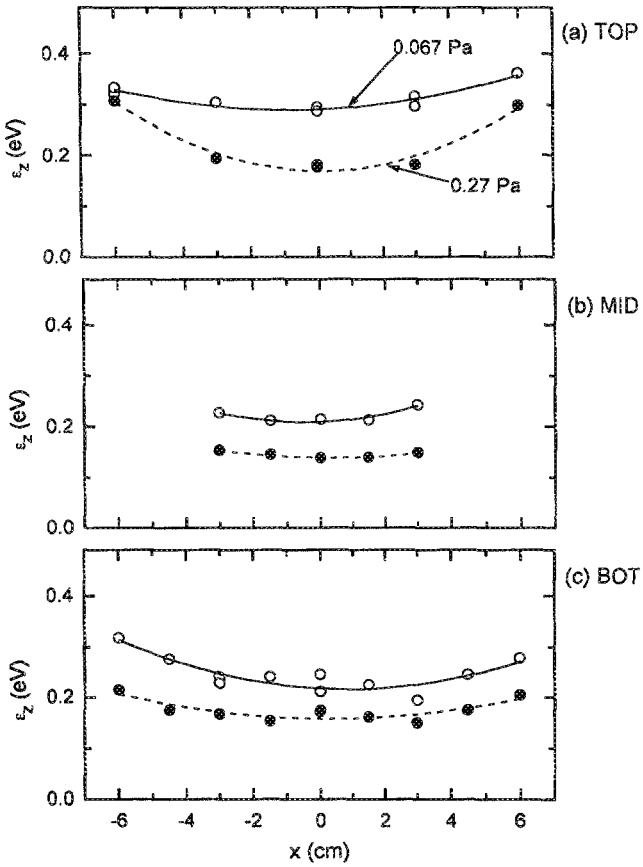

FIG. 18. Random parallel ion energy ε_z as a function of x and z for two different pressures in the double-cusp configuration.

2. Double-cusp configuration

The consequences of changing the magnetic field configuration on the v_z ivdf are dramatic as shown in Fig. 13. First, the reversal in the direction of ion drift is shifted from between the TOP and MID positions to between the MID and BOT positions. This is precisely how the maximum in the magnetic field shifts, again indicating that the plasma potential and density tend to be largest where the magnetic field is strongest. Second, because the magnetic field is more uniform at the BOT position in the double-cusp configuration, the ivdf is no longer bimodal and both the average velocity and the random energy decrease (Figs. 16–18). Comparing the radial spatial profiles of $\langle v_z \rangle$ and ε_z for the mirror and double-cusp configurations, we see that the double-cusp plasma is more uniform in both $\hat{x}$ and $\hat{z}$ and the velocity spread along $\hat{z}$ is reduced as a consequence.

As the pressure is increased, the improved plasma uniformity in the double-cusp configuration is clearly evident in the systematic reduction in both $\langle v_z \rangle$ and ε_z (Fig. 16). Since the plasma is initially uniform, compared to the mirror configuration, the drift velocities are small on-axis. By increasing the pressure, the plasma uniformity is not degraded significantly and the elastic and charge exchange collisions simply slow and cool the ions.

IV. CONCLUSIONS

We have used Doppler-shifted laser-induced fluorescence and microwave interferometry to measure metastable ion velocity distributions and electron densities in helicon-wave plasmas as a function of magnetic field and pressure.

We find that the plasma density in the middle of the source is always larger for the double-cusp configuration for the same power and pressure as in the mirror field configuration. This enhancement in density is consistent with reduction in wall loss by improved magnetic confinement. The plasma symmetry and uniformity are also improved in the double-cusp configuration. The origin of the asymmetry in the mirror configuration is not understood but clearly implies asymmetric ionization and as such is likely dependent on the details of helicon wave excitation and damping.

Because of plasma nonuniformity and collisions, linewidth control in the mirror configuration is expected to be most difficult to achieve at intermediate pressures: Either decreasing or increasing the pressure should be beneficial when etching is limited by ion energy flux to the wafer surface. By contrast, in the double-cusp configuration, etching linewidth control should be easiest to achieve at *higher* pressures where the transverse ion energy is reduced by collisions with neutrals.

[1]J. M. Cook and K. G. Donohoe, Solid State Technol. **34**, 119 (1991).
[2]P. H. Singer, Semicond. Int. **46** (1991).
[3]D. L. Flamm, Solid State Technol. **14**, 47 (1991).
[4]K. Suzuki, K. Ninomiya, S. Nishimatsu, and S. Okudaira, J. Vac. Sci. Technol. B **3**, 1025 (1985); K. Suzuki, S. Okudaira, and I. Kanomata, J. Electrochem. Soc. **126**, 1024 (1979).
[5]M. A. Lieberman and R. A. Gottscho, *Physics of Thin Films: Advances in Research and Development*, edited by J. Vossen (Academic, New York, 1993), Vol. 17.
[6]E. S. G. Shaqfeh and C. W. Jurgensen, J. Appl. Phys. **66**, 4664 (1989).
[7]R. A. Gottscho, J. Vac. Sci. Technol. B **11**, 1884 (1993).
[8]D. J. Trevor, N. Sadeghi, T. Nakano, J. Derouard, R. A. Gottscho, P. D. Foo, and J. M. Cook, Appl. Phys. Lett. **57**, 1188 (1990); T. Nakano, N. Sadeghi, and R. A. Gottscho, Appl. Phys. Lett. **58**, 458 (1991); N. Sadeghi, T. Nakano, D. J. Trevor, and R. A. Gottscho, J. Appl. Phys. **70**, 2552 (1991); N. Sadeghi, T. Nakano, D. J. Trevor, and R. A. Gottscho, J. Appl. Phys. **71**, 3648 (1992); T. Nakano, N. Sadeghi, D. J. Trevor, R. A. Gottscho, and R. W. Boswell, J. Appl. Phys. **72**, 3384 (1992).
[9]T. Nakano, R. A. Gottscho, N. Sadeghi, D. J. Trevor, R. W. Boswell, A. J. Perry, T. C. Lee, K. P. Giapis, and J. Margot, Jpn. Soc. Appl. Phys. **61**, 711 (1992).
[10]R. Koslover and R. McWilliams, Rev. Sci. Instrum. **57**, 2441 (1986); R. McWilliams and M. Okubo, Phys. Fluids **30**, 2849 (1987); R. McWilliams, M. K. Okubo, and N. S. Wolf, Phys. Fluids B **2**, 523 (1990).
[11]R. K. Porteous and D. B. Graves, IEEE Trans Plasma Sci. **PS-19**, 204 (1991); R. K. Porteous, H.-M. Wu, and D. B. Graves, Plasma Sources Technol. (in press).
[12]P. L. G. Ventzek, R. J. Hoekstra, T. J. Sommerer, and M. J. Kushner, Appl. Phys. Lett. **63**, 605 (1993).
[13]See for example, T. Arikado, K. Horioka, M. Sekine, H. Okano, and Y. Horiike, Jpn. J. Appl. Phys. **27**, 95 (1988); S. Kato, M. Sato, and Y. Arita, 1989 Dry Proceedings Symposium Tokyo, 1989 (unpublished), p. 33; J. Ulacia, C. J. Petti, and J. P. McVittie, J. Electrochem. Soc. **135**, 1521 (1988).
[14]R. C. Woods, R. L. McClain, L. J. Mahoney, E. A. Den Hartog, H. Persing, and J. S. Hamers, SPIE **1594**, 366 (1991); E. A. Den Hartog, H. Persing, J. S. Hamers, and R. C. Woods, 10th International Symposium on Plasma Chemical, Bochum, Germany, 4–9 August, 1991 (unpublished); E. A. Den Hartog, H. Persing, J. S. Hamers, and R. Claude Woods, 44th Gaseous Electronics Conference, Albuquerque, NM, October 1991 (unpublished), Abstract DA-1.
[15]K. P. Giapis, N. Sadeghi, J. Margot, R. A. Gottscho, and T. C. Lee, J. Appl. Phys. **73**, 7188 (1993).
[16]J. Hopwood, Plasma Sources Sci. Technol. **1**, 109 (1992).
[17]R. Bowers, C. Legendy, and F. E. Rose, Phys. Rev. Lett. **7**, 339 (1961).
[18]G. N. Harding and P. C. Thonemann, Proc. Phys. Soc. **85**, 301 (1965).
[19]J. C. Woods, J. Fluid Mech. **13**, 570 (1962).
[20]J. P. Klosenberg, B. McNamara, and P. C. Thonemann, J. Fluid Mech. **21**, 545 (1965).
[21]R. W. Boswell, Ph.D. thesis, Flinders University of South Australia (1970).
[22]R. W. Boswell, Phys. Lett. A **33**, 457 (1970).
[23]F. F. Chen, Laser Part. Beams **7**, 551 (1989).
[24]F. F. Chen, Plasma Phys. Contr. Fusion **33**, 339 (1991).
[25]A. Komori, T. Shoji, K. Miyamoto, J. Kawai, and K. Kawai, Phys. Fluids B **3**, 893 (1991).
[26]P. K. Lowenhardt, B. D. Blackwell, R. W. Boswell, G. D. Conway, and S. M. Hamberger, Phys. Rev. Lett. **67**, 2792 (1991).
[27]A. Bouchoule, P. Ranson, and D. Henry, French Patent No. 83 18300 (1983); D. Henry, J. M. Francou, and A. Inard, J. Vac. Sci. Technol. A **10**, 3426 (1992).
[28]R. W. Boswell and R. K. Porteous, J. Appl. Phys. **62**, 3123 (1987).
[29]A. J. Perry and R. W. Boswell, Appl. Phys. Lett. **55**, 148 (1989).
[30]P. Boyer, Ph.D. thesis, L'Institut National des Sciences Appliquees de Toulouse, January 28, 1993.
[31]G. Campbell (unpublished results).
[32]R. Petri, J. Appl. Phys. **72**, 2644 (1992).
[33]F. F. Chen, J. Vac. Sci. Technol. A **10**, 1389 (1992).
[34]T. C. Lee, R. A. Gottscho, K. P. Giapis, T. Nakano, N. Sadeghi, and J. Margot, Proceedings of the 39th National Symposium of the American Vacuum Society, Chicago, IL, 9–13 November 1992 (unpublished).
[35]C. Charles, R. W. Boswell, and R. K. Porteous, J. Vac. Sci. Technol. A **10**, 398 (1992).
[36]A. R. Ellingboe and R. W. Boswell, 45th Gaseous Electronics Conference, Boston, MA, October 1992 (unpublished), Abstract LB-1.